Nanoscale Advances

ROYAL SOCIETY OF CHEMISTRY

PAPER

View Article Online
View Journal | View Issue

Check for updates

Cite this: *Nanoscale Adv.*, 2020, **2**, 1646

The rational design of carbon coated $Fe_2(MoO_4)_3$ nanosheets for lithium-ion storage with high initial coulombic efficiency and long cycle life†

Chennan Liang, Yuanxue Tao, Dekang Huang, Shu Li, Feifei Cao, Yanzhu Luo* and Hao Chen*

Received 12th February 2020
Accepted 7th March 2020

DOI: 10.1039/d0na00122h

rsc.li/nanoscale-advances

Binary metal oxides are potential anode materials for lithium-ion storage due to their high theoretical specific capacities. However, the practical applications of metal oxides are limited due to their large volume changes and sluggish reaction kinetics. Herein, carbon coated $Fe_2(MoO_4)_3$ nanosheets are prepared *via* a simple method, adopting urea as the template and carbon source. The carbon coating on the surface helps to elevate the conductivity of the active material and maintain structural integrity during the lithium storage process. Combining this with a catalytic effect from the generated Fe, leading to the reversible formation of a solid electrolyte interface layer, a high initial coulombic efficiency (>87%) can be obtained. Based on this, the carbon coated $Fe_2(MoO_4)_3$ nanosheets show excellent rate capability (a reversible discharge capacity of 983 mA h g^{-1} at 5 A g^{-1}) and stable cycling performance (1376 mA h g^{-1} after 250 cycles at 0.5 A g^{-1} and 864 mA h g^{-1} after 500 cycles at 2 A g^{-1}). This simple *in situ* carbonization and template method using urea provides a facile way to optimize electrode materials for next-generation energy storage devices.

1. Introduction

The rapidly increasing demand for energy-storage systems for electric vehicles (EVs) and stationary systems has triggered large numbers of investigations into novel lithium ion batteries (LIBs) with high energy densities, high rate performances, and good safety characteristics. The exploration of new anode materials is the most significant way to elevate the performances of LIBs.[1] Compared with current commercial graphite anodes with a low theoretical capacity of 372 mA h g^{-1},[2] conversion electrodes have drawn great attention as a result of their higher theoretical capacities.[3,4] Among the various electrode candidates, mixed metal oxides are expected to offer excellent redox performance due to a synergistic effect from the constituent metal ions, which can improve the reversible charge/discharge capacities, electrical/ionic conductivities, and mechanical stabilities of the electrode materials.[5–8]

$Fe_2(MoO_4)_3$ is an important anode electrode material for lithium-ion batteries; molybdenum six-electron transfer and iron three-electron transfer can deliver a high theoretical capacity of 1087 mA h g^{-1}.[9–11] During the initial discharge process, $Fe_2(MoO_4)_3$ irreversibly decomposes into iron, molybdenum, and Li_2O upon lithiation, then transforms into iron oxide and molybdenum oxide upon delithiation. Tarascon's group observed that newly generated metal nanoparticles from metal oxides could serve as effective catalysts to activate and promote the reversible formation/decomposition of a solid-electrolyte interface (SEI) layer.[12] Zhou's group also discovered that *in situ* formed Fe nanoclusters can act as an effective catalyst for the formation of some SEI components, leading to improved initial coulombic efficiency (ICE) values for electrode materials, as well as extra capacity due to reversible conversion reactions.[13]

Thus, it is obvious that $Fe_2(MoO_4)_3$ is a potential anode material for LIBs due to its high theoretical capacity and improved ICE. However, it also suffers from large volume changes along with lithium insertion/deinsertion behavior, leading to the loss of electrical contact with current collectors and continuous capacity loss. In addition, $Fe_2(MoO_4)_3$ suffers from sluggish reaction kinetics due to its intrinsic semiconducting nature, which also needs to be effectively addressed.[11] In order to solve the issues mentioned above, various methods have been proposed, including developing nanomaterials with much reduced numbers of Li^+ diffusion pathways, and combination with highly conductive materials (such as carbon materials).[14,15] Qian *et al.* synthesized $FeMoO_4$ nanocubes with a high specific discharge capacity of 926 mA h g^{-1} at 100 mA g^{-1} after 80 cycles.[16] Three-dimensional $Fe_2(MoO_4)_3$ microspheres with ultrathin nanosheet constituents were first synthesized by Zheng *et al.*, delivering a high initial capacity (1855 mA h g^{-1} at 100 mA g^{-1}) and stable cycling

College of Science, Huazhong Agricultural University, Wuhan 430070, PR China. E-mail: hchenhao@mail.hzau.edu.cn; luoyanzhu@mail.hzau.edu.cn

† Electronic supplementary information (ESI) available. See DOI: 10.1039/d0na00122h

performance (456 mA h g^{-1} over 50 cycles at 800 mA g^{-1}).[17] Pramanik *et al.* reported the fabrication of $Fe_2(MoO_4)_3$/MWCNT nanocomposites, which delivered a high specific capacity of 600 mA h g^{-1} at a high current density of 1200 mA g^{-1}.[9] As a consequence, it is obvious that the modification methods mentioned above could effectively improve the electrochemical performance of the active material. However, it is worth noting that the ICE values of the $Fe_2(MoO_4)_3$ active materials reported previously are almost always less than 80%,[9–11] as nanoscale materials with large numbers of reaction sites present the possibility for numerous side reactions with the electrolyte, leading to reduced ICE values.

Furthermore, it has been reported that the direct coating of active materials with carbon is supposed to promote the ion/electron diffusion coefficient and reduce structural expansion during the electrochemical process, leading to a higher ICE.[18] In this work, carbon coated $Fe_2(MoO_4)_3$ nanosheets ($Fe_2(MoO_4)_3$/C-NS) were synthesized through a facile solution method combined with calcination treatment, using urea as the template and carbon source. As-prepared $Fe_2(MoO_4)_3$/C-NS presents a 2D structure, suitable surface area, and uniform carbon coating, which are beneficial for ion/electron transfer and ICE improvement. As expected, a purposefully designed $Fe_2(MoO_4)_3$/C-NS electrode exhibited much improved electrochemical performance (a high reversible capacity of 1376 mA h g^{-1} after 250 cycles at 0.5 A g^{-1}, excellent rate performance of 983 mA h g^{-1} at 5 A g^{-1}, and an ICE higher than 87%) compared with $Fe_2(MoO_4)_3$ microparticles ($Fe_2(MoO_4)_3$-MP, synthesized without urea), making this a potential anode material for next-generation LIBs. This work also demonstrates a facile way to develop high-performance electrode materials *via* the construction of heterostructures through the *in situ* carbonization of urea.

2. Experimental section

2.1 Synthesis

For the synthesis of $Fe_2(MoO_4)_3$/C-NS, 0.8080 g of $Fe(NO_3)_3 \cdot 9H_2O$ was dispersed in 18 mL of deionized water, and 0.3531 g of $(NH_4)_6Mo_7O_{24} \cdot 4H_2O$ was dispersed in 20 mL of deionized water; these were separately magnetically stirred for 10 minutes to get homogeneous solutions. Subsequently, the $Fe(NO_3)_3 \cdot 9H_2O$ solution was slowly added into the $(NH_4)_6Mo_7O_{24} \cdot 4H_2O$ solution. Then 2 mL of HNO_3 and 1 g of urea were added to get the precursor solution. The precursor solution was continuously stirred for 5 h, and it was transferred into a drying oven and held at 140 °C to evaporate the water. After this, the collected precursor powder was put into a 30 mL alumina crucible with a cover, then annealed at 500 °C for 10 h in air at a heating rate of 5 °C min^{-1} to get $Fe_2(MoO_4)_3$/C-NS. The control sample of $Fe_2(MoO_4)_3$ microparticles was synthesized *via* the same procedure without the addition of urea.

2.2 Material characterization

Sample crystal structures were obtained using X-ray powder diffraction (XRD) analysis (Bruker D8 Discover) with Cu Kα radiation. Sample morphologies and elemental compositions were studied using a JEOL JSM-7100F scanning electron microscope (SEM) equipped with an energy dispersive spectrometer (EDS) and a JEOL JEM-2100F high-resolution transmission electron microscope (HRTEM). The specific surface areas (Brunauer–Emmett–Teller (BET) model) and pore size distributions (Barrett–Joyner–Halenda (BJH) model) of the samples were measured at 77 K (Micromeritics Tristar 3020). X-ray photoelectron spectroscopy (XPS) analysis was carried out using Thermo Scientific Escalab 250Xi apparatus. Raman signals were collected using a microscopic confocal Renishaw 1000 NR Raman spectrometer. Thermogravimetric (TG) analysis was carried out using a thermal gravimetric analyzer (NETZSCH TG209) from 30 to 800 °C at a heating rate of 10 °C min^{-1} under the air atmosphere. Fourier transform infrared spectra (FT-IR) were collected using a Nicolet iS50 FT-IR spectrometer.

2.3 Electrochemical measurements

CR2016 coin cells were assembled in a glove box (argon atmosphere), and their electrochemical performance was evaluated using a NEWARE CT2001A battery testing system. The working electrode slurry was composed of 70 wt% active material, 20 wt% acetylene black, and 10 wt% sodium alginate, and it was coated onto copper foil. The slurry was dried at 60 °C, then the electrode film was punched into circular disks. The electrolyte was composed of 1 M $LiPF_6$ in ethylene carbon (EC)/dimethyl carbonate (DMC) (1 : 1 by volume) with 5% fluoroethylene carbonate (FEC). Cyclic voltammetry (CV) and electrochemical impedance spectroscopy (EIS) measurements were carried out using an electrochemical workstation (CHI 760D).

3. Results and discussion

During the synthesis process, transparent yellow $Fe(NO_3)_3 \cdot 9H_2O$ solution and colorless $(NH_4)_6Mo_7O_{24} \cdot 4H_2O$ solution can be obtained after dissolution in deionized water (Fig. S1A and B†). A yellow precipitate appears after mixing $Fe(NO_3)_3 \cdot 9H_2O$ and $(NH_4)_6Mo_7O_{24} \cdot 4H_2O$ (Fig. S1C†), which quickly dissolves after adding 2 mL of HNO_3 (Fig. S1D†). As shown in Fig. S2A and B,† the yellow precipitate has an irregular solid structure and is made up of Fe, Mo, and O elements (EDS results in Fig. S2C†). The absence of characteristic peaks indicates the amorphous character of the yellow precipitate (Fig. S3†). However, as mentioned, the yellow precipitate quickly dissolves after the introduction of 2 mL of HNO_3 (Fig. S1D†), and the transparent light-yellow solution does not change after the addition of urea (Fig. S1E†). After the drying and air-calcination processes, $Fe_2(MoO_4)_3$/C-NS and $Fe_2(MoO_4)_3$-MP materials can be obtained with and without urea, respectively. According to the XRD patterns in Fig. 1A, all characteristic peaks can be indexed to monoclinic $Fe_2(MoO_4)_3$ (JCPDS no. 01-083-1701), without any impurities. It is interesting that urea plays a key role in determining the final morphology of the obtained material, acting as the template and carbon source during the fabrication process. The SEM image in Fig. 1B reveals that with the assistance of urea, $Fe_2(MoO_4)_3$/C-NS presents a uniform nanosheet structure.

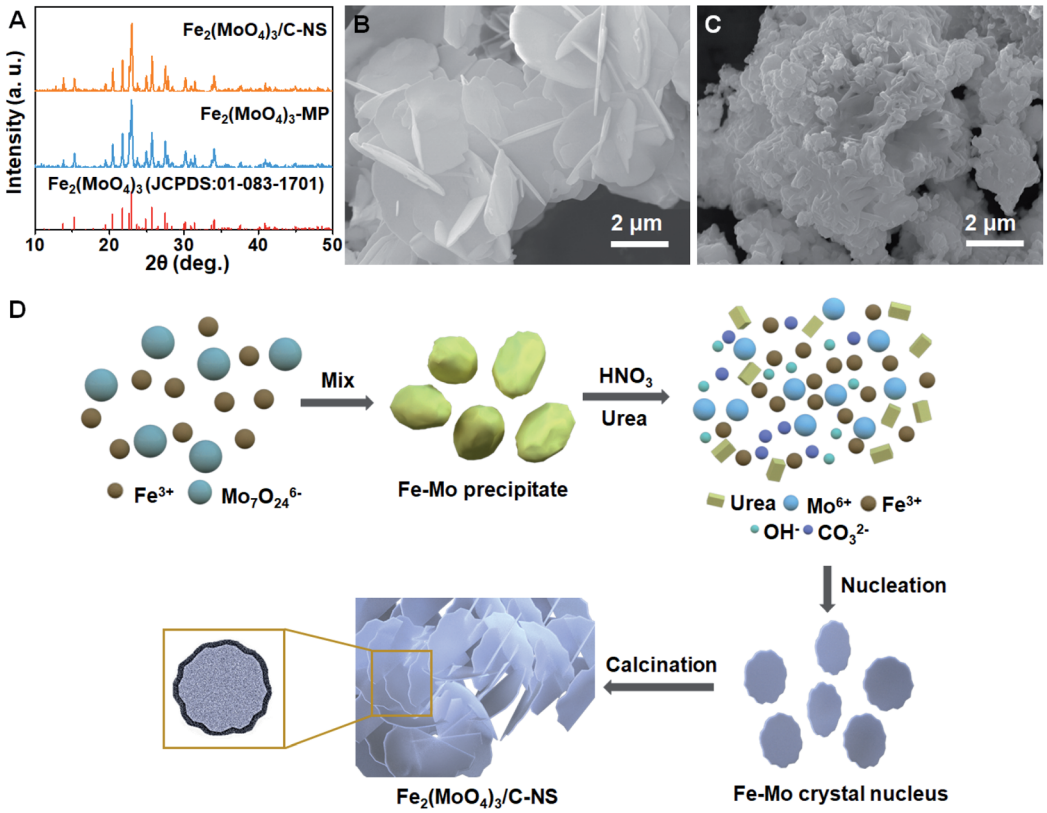

Fig. 1 (A) XRD patterns of $Fe_2(MoO_4)_3$/C-NS and $Fe_2(MoO_4)_3$-MP; and SEM images of $Fe_2(MoO_4)_3$/C-NS (B) and $Fe_2(MoO_4)_3$-MP (C). (D) The proposed mechanism for the synthesis of $Fe_2(MoO_4)_3$/C-NS.

However, without the effects of the urea template, $Fe_2(MoO_4)_3$-MP is composed of irregular particles (Fig. 1C).

Based on the above experimental results, a synthetic mechanism diagram for $Fe_2(MoO_4)_3$/C-NS is illustrated in Fig. 1D. The yellow precipitate consisting of Fe, Mo, and O elements appears quickly after mixing the $Fe(NO_3)_3 \cdot 9H_2O$ and $(NH_4)_6Mo_7O_{24} \cdot 4H_2O$ aqueous solutions, and it dissolves into solution upon further reaction with HNO_3. When drying at 140 °C, H_2O and excess HNO_3 evaporate, while urea decomposes into CO_3^{2-} and OH^- slowly, distributing uniformly throughout the solution. Subsequently, Fe–Mo nuclei are precipitated through a reaction between Fe^{3+} and Mo^{6+} and the generated anions (CO_3^{2-} and OH^-), and grow into nanosheets gradually (Fig. S4A†).[19,20] Then some of the remaining urea can act as the carbon source due to the semi-closed reaction system existing in the furnace, while the rest completely decomposes into NH_3 and CO_2 molecules, which can effectively reduce the aggregation of nanosheets in the subsequent calcination process.[21] The characteristic FT-IR peaks of the $Fe_2(MoO_4)_3$/C-NS precursor confirm the existence of excess urea after the drying process. The series of peaks from 1800 to 1000 cm^{-1} can be ascribed to the stretching vibrations of C–N heterocycles, while the peaks from 3300 to 3000 cm^{-1} can be assigned to the stretching vibration modes of N–H and O–H bonds (Fig. S5A†), both of which completely disappear after the calcination process (Fig. S5B†).[22] The greater weight loss from the $Fe_2(MoO_4)_3$/C-NS precursor also confirms the decomposition of urea during the calcination process (Fig. S6†). Only microparticles can be obtained without the urea template (Fig. S4B†), and their diameter further increases during the high-temperature calcination procedure.

The results obtained from high-angle annular dark field (HAADF) imaging show that the surface of $Fe_2(MoO_4)_3$/C-NS is covered by a uniform carbon layer; this is further confirmed from the elemental mapping images (Fig. 2A). An EDS line scan (Fig. 2B and C) further confirms that the outermost layer is composed of pure carbon. From transmission electron microscopy (TEM) imaging, it can be observed that $Fe_2(MoO_4)_3$/C-NS displays typical sheet-like morphology, and the low contrast indicates the ultrathin properties of the nanosheets (Fig. 2D). Selective area electron diffraction (SAED) studies were performed on a typical nanosheet, revealing its single-crystalline nature and good crystallinity (the inset of Fig. 2D). The uniform carbon coating can also be confirmed from the high resolution TEM image in Fig. S7,† and the regular lattice fringes with spacings of 0.39 and 0.63 nm can be ascribed well to the (202) and (200) planes of $Fe_2(MoO_4)_3$ (Fig. 2E).

The elemental composition of $Fe_2(MoO_4)_3$/C-NS was examined *via* XPS, and the results are shown in Fig. 2F–H and S8.† The high-resolution Fe 2p peaks (Fig. 2F) can be deconvoluted to $2p_{1/2}$ (725.3 eV) and $2p_{3/2}$ (711.5 eV) peaks from Fe^{3+}, and corresponding satellite peaks.[23] The high-resolution Mo 3d peaks (Fig. 2G) originating at 232.2 and 235.3 eV correspond to $3d_{5/2}$ and $3d_{3/2}$ peaks of Mo^{6+}, respectively.[24] The O 1s peak centered at 530.4 eV is assigned to the formation of lattice oxygen, and the peak centered at 532.2 eV is attributed to

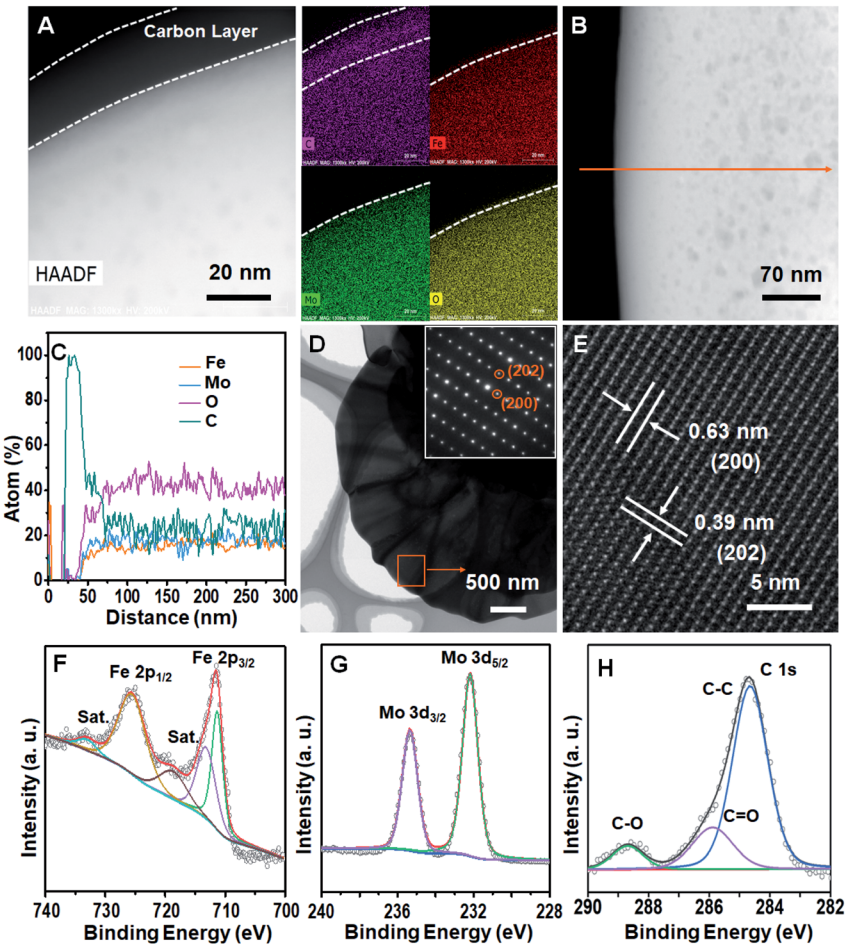

Fig. 2 A HAADF image and elemental mapping (A) of $Fe_2(MoO_4)_3$/C-NS; a HAADF image (B) and the corresponding EDS line scan (C) of $Fe_2(MoO_4)_3$/C-NS; a TEM image (D), an SAED pattern (the inset of (D)), and a HRTEM image (E) of $Fe_2(MoO_4)_3$/C-NS; high-resolution Fe 2p (F), Mo 3d (G), and C 1s (H) XPS spectra of $Fe_2(MoO_4)_3$/C-NS.

surface oxygen (Fig. S8†).[25] The peaks in the C 1s fitted spectra located at 284.6, 285.9, and 288.5 eV for $Fe_2(MoO_4)_3$/C-NS are assigned to C–C, C═O and C–O, respectively (Fig. 2H).[26]

N_2 adsorption isotherm analysis was conducted to explore the surface areas and BJH pore size distributions of $Fe_2(MoO_4)_3$/C-NS and $Fe_2(MoO_4)_3$-MP (Fig. S9†). Both showed type-IV sorption isotherms with type-H4 hysteresis loops, indicating the existence of mesopores in the samples, which may be accumulated by primary nanosheets or nanoparticles.[27] $Fe_2(MoO_4)_3$/C-NS (11.0 $m^2\ g^{-1}$) exhibits a similar specific surface area to $Fe_2(MoO_4)_3$-MP (10.9 $m^2\ g^{-1}$), and this appropriate specific surface area could reduce the numbers of irreversible reactions between the electrolyte and active material, leading to an improved ICE value.

The lithium insertion/deinsertion behaviors of $Fe_2(MoO_4)_3$/C-NS and $Fe_2(MoO_4)_3$-MP during the first cycle were studied *via* cyclic voltammetry at a sweep rate of 0.1 mV s^{-1} in the range of 0.01–3.0 V (Fig. 3A). Though both samples demonstrate similar redox behavior, the current densities of the redox peaks of $Fe_2(MoO_4)_3$/C-NS are slightly higher than those of $Fe_2(MoO_4)_3$-MP, indicating the higher electrochemical reaction activity of $Fe_2(MoO_4)_3$/C-NS.[28] The peaks centered at 2.95 and 1.50 V are ascribed to multi-step Li^+ insertion into the $Fe_2(MoO_4)_3$ crystal lattice, resulting in the formation of $Li_xFe_2(MoO_4)_3$.[11] The two reduction peaks at 1.2 V and 0.7 V can be attributed to the decomposition of $Li_2Fe_2(MoO_4)_3$ into $Li_2Fe_3O_5$ and Li_2MoO_3. With further lithium insertion, the reduction peak at 0.3 V can be attributed to the formation of a SEI and the conversion of $Li_2Fe_3O_5$ and Li_2MoO_3 to metallic Fe^0 and Mo^0, along with the generation of a Li_2O matrix.[10] During the charging process, the oxidation peak at 0.50 V indicates the oxidation of Mo^0 to Mo^{6+}, and the oxidation peaks located at 1.65 and 1.83 V are ascribed to the conversion of Fe^0 to Fe^{3+}.[9] Due to the irreversible structural transformation of the active material during the first cycle, subsequent electrochemical reactions are different to the first cycle. During the second cycle, reduction peaks located at 0.24, 0.76, and 1.59 V are observed (Fig. S10A†). The peak at 1.59 V can be attributed to the initial lithiation of MoO_3 along with the formation of Li_xMoO_3, while the peak at 0.24 V represents the reduction of Li_xMoO_3 to Mo^0 and Li_2O. The peak at 0.76 V is due to the reduction of Fe^{2+} or Fe^{3+} to Fe^0.[9,16,29] The CV curves of $Fe_2(MoO_4)_3$/C-NS at sweep rates from 0.1 to 5.0 mV s^{-1} were further investigated, as shown in Fig. S10B.† Even at a high sweep rate of 5.0 mV s^{-1}, the reduction/oxidation peaks could

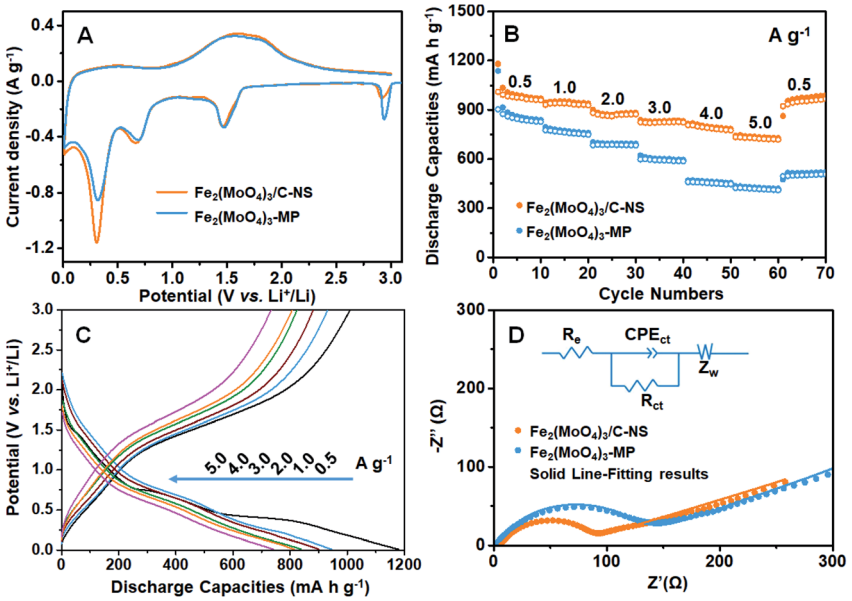

Fig. 3 (A) Curves from the first CV cycles of $Fe_2(MoO_4)_3$/C-NS and $Fe_2(MoO_4)_3$-MP at a sweep rate of 0.1 mV s^{-1} from 0.01–3.0 V. (B) The rate performances of $Fe_2(MoO_4)_3$/C-NS and $Fe_2(MoO_4)_3$-MP at varied rates from 0.5 to 5 A g^{-1}. (C) The discharge–charge voltage profiles of $Fe_2(MoO_4)_3$/C-NS at current densities from 0.5 A g^{-1} to 5 A g^{-1}. (D) Nyquist plots of $Fe_2(MoO_4)_3$/C-NS and $Fe_2(MoO_4)_3$-MP before cycling.

be clearly observed, demonstrating the superior rate performance of $Fe_2(MoO_4)_3$/C-NS.[30,31]

The rate capabilities of $Fe_2(MoO_4)_3$/C-NS and $Fe_2(MoO_4)_3$-MP for lithium storage were comparatively investigated at different current densities (Fig. 3B). As expected, $Fe_2(MoO_4)_3$/C-NS displays extraordinarily high reversible discharge capacities of 1035, 949, 883, 832, 819, and 744 mA h g^{-1} from 0.5 to 5.0 A g^{-1}. Remarkably, a high discharge capacity of 955 mA h g^{-1} could be recovered when the current density was returned to 0.5 A g^{-1}, showing the existence of a stable structure at a high current density. However, $Fe_2(MoO_4)_3$-MP shows much inferior discharge capacities of 914, 785, 698, 611, 469, and 434 mA h g^{-1} at the same current densities, as well as a low recovered discharge capacity of 514 mA h g^{-1} at 0.5 A g^{-1}. This electrochemical comparison clearly indicates the structural superiority of the obtained $Fe_2(MoO_4)_3$/C-NS, as the carbon layer could effectively promote charge transfer during the reaction process, elevate the rate performance to a high level, and maintain the structural integrity of the electrode material.[32] Moreover, the first galvanostatic charge/discharge curves of $Fe_2(MoO_4)_3$/C-NS from 0.5 to 5.0 A g^{-1} are exhibited in Fig. 3C. Irreversible structural change could be observed, as the initial discharge curve at 0.5 A g^{-1} is totally different from the others; this is in accordance with the CV results. Even at a high current density of 5.0 A g^{-1}, curve plateaus are obvious during the discharge/charge process, indicating that $Fe_2(MoO_4)_3$/C-NS exhibits superior rate capabilities compared to $Fe_2(MoO_4)_3$-MP (Fig. S11†).[33] The idea that the carbon layer coating can increase the conductivity of $Fe_2(MoO_4)_3$/C-NS is further confirmed from electrochemical impedance spectroscopy (EIS) measurements at 3.0 V. Nyquist plots of fresh $Fe_2(MoO_4)_3$/C-NS and $Fe_2(MoO_4)_3$-MP electrodes are compared in Fig. 3D. Both of the Nyquist plots exhibit semicircles in the medium frequency region, which are related to interfacial charge transfer processes. The sloped lines in the low frequency regions could be related to lithium diffusion processes. Zview software was applied to fit the obtained data, and the equivalent circuit is presented in the inset of Fig. 3D; the R_{ct} values of $Fe_2(MoO_4)_3$/C-NS and $Fe_2(MoO_4)_3$-MP are fitted as 66.5 Ω and 110 Ω, respectively, indicating that the coated carbon layer and nanosheet structure could significantly enhance the electronic conductivity of $Fe_2(MoO_4)_3$/C-NS. A new semicircle in the high frequency appeared after the electrochemical reaction, which is ascribed to the formation of a SEI layer (Fig. S12†). Based on the equivalent circuit, the R_f and R_{ct} values after five cycles were fitted as 25.0 and 35.6 Ω, respectively, which are quite close to the values after one cycle (R_f: 26.3 Ω; R_{ct}: 33.8 Ω), demonstrating the stable interface and host structure of $Fe_2(MoO_4)_3$/C-NS.

The cycling performances and corresponding initial coulombic efficiencies of the electrodes are investigated based on a half-cell configuration from 0.01 to 3.0 V (*vs.* Li^+/Li) at current densities of 0.5, 2, and 5 A g^{-1} (Fig. 4A). High initial discharge capacities of 1230, 1147, and 1115 mA h g^{-1} can be observed at 0.5, 2, and 5 A g^{-1}, with high ICE values of 87%, 92%, and 87%, respectively (Fig. 4C). It is worth noting that these ICE values are much higher than those reported for other metal oxide electrodes.[34–38] It is obvious that the discharge capacities of $Fe_2(MoO_4)_3$/C-NS are higher than the theoretical capacity, as has been reported for oxide materials previously.[9,11] This phenomenon can be attributed to the formation of a SEI layer, surface pseudocapacitance, the defect-induced storage of lithium ions, *etc.*[10] The discharge capacity finally stabilizes at 1376 mA h g^{-1} at 0.5 A g^{-1} after 250 cycles, and a high discharge capacity of 864 mA h g^{-1} is shown at 2 A g^{-1} after 500 cycles. Even at a high current density of 5 A g^{-1}, a stable specific capacity of 484 mA h g^{-1} can be obtained after 1000 cycles, corresponding to capacity retention of 49.2% compared with the

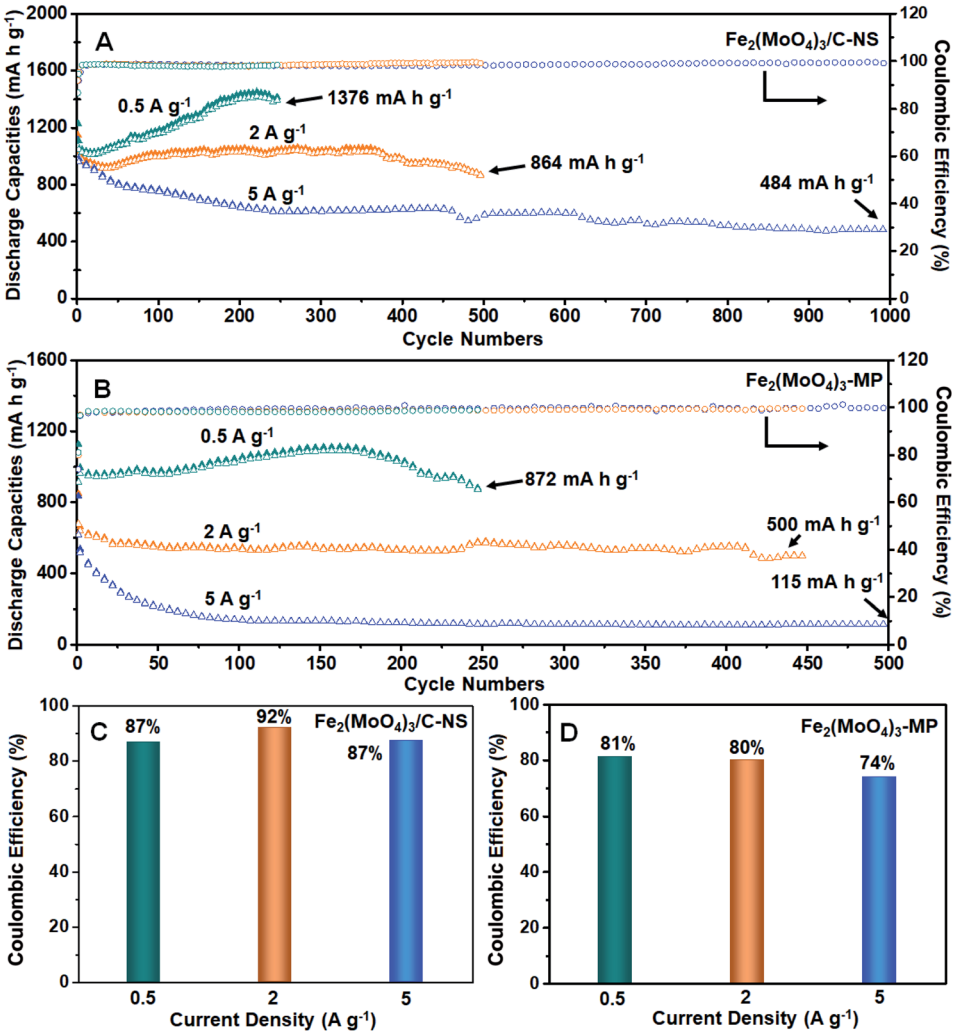

Fig. 4 The cycling performances of $Fe_2(MoO_4)_3$/C-NS (A) and $Fe_2(MoO_4)_3$-MP (B) at current densities of 0.5, 2, and 5 A g^{-1}. The ICEs of $Fe_2(MoO_4)_3$/C-NS (C) and $Fe_2(MoO_4)_3$-MP (D) at 0.5, 2, and 5 A g^{-1}.

second cycle discharge capacity (983 mA h g^{-1}). However, $Fe_2(MoO_4)_3$-MP delivers inferior initial discharge capacities of 1127, 848, and 834 mA h g^{-1} at 0.5, 2, and 5 A g^{-1} (Fig. 4B), along with low ICE values of 81%, 80%, and 74% (Fig. 4D), respectively. The excellent performance, with high specific capacity, high ICE, and excellent cycling performance, can be attributed to the special structure of $Fe_2(MoO_4)_3$/C-NS, as the well-dispersed nanosheet structure can provide more channels with short diffusion distances for reactions related to Li^+ insertion/extraction. At the same time, the outer carbon layer can minimize the electronic resistance, guaranteeing more homogeneous volume variations during the electrochemical processes and thereby leading to superior electrochemical performance.[39–41]

In order to investigate the interface reactions, EIS spectra from the $Fe_2(MoO_4)_3$/C-NS electrode in fully charged/discharged states relating to the first, second, and third cycles are shown in Fig. 5A. Two semicircles could be observed in the EIS curves in Fig. 5A; the semicircle in the high frequency region corresponds to the formation of a SEI layer (R_f), while the semicircle located in the medium frequency region could be ascribed to charge transfer resistance (R_{ct}). According to the equivalent circuit in Fig. 5A, the R_f value after the first discharge cycle is fitted as 81.5 Ω, which decreases to 26.5 Ω after the charging process. This same phenomenon can also be observed during the second and third cycles, indicating the highly reversible transformation of the SEI layer during the charge/discharge process (Table S1†). Furthermore, FT-IR analysis was conducted to explore the chemical states of $Fe_2(MoO_4)_3$/C-NS in different charge (3.0 V) and discharge (2.5, 1.0, 0.5, and 0.01 V) states (Fig. 5B). Compared with the fresh electrode, some characteristic peaks gradually appear. The peaks at 1330 and 1406 cm^{-1} can be ascribed to the formation of $ROCO_2Li$,[42,43] and the strong peak at 1405 cm^{-1} corresponds to the formation of Li_2CO_3.[44] When the electrode is further discharged to 0.5 V, a new peak at around 3675 cm^{-1} is formed, indicating the formation of LiOH.[45] This experimental phenomenon confirms the formation of a SEI layer during the discharge process, as $ROCO_2Li$, Li_2CO_3, and LiOH are major constituents of the SEI layer. Upon charging to 3.0 V, the LiOH peak disappears and the intensities of the other peaks reduce, demonstrating the partial decomposition of the SEI layer. In the discharge process, initial $Fe_2(MoO_4)_3$ is converted to Fe and Mo nanocrystals. It has been reported that Fe can function as a kind

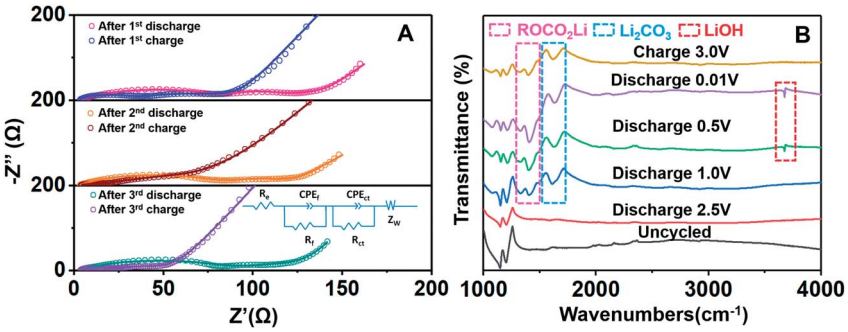

Fig. 5 (A) EIS spectra from the $Fe_2(MoO_4)_3$/C-NS electrode in fully charged/discharged states relating to the first, second, and third cycles. (B) FT-IR spectra of $Fe_2(MoO_4)_3$/C-NS in different charge/discharge states from the first cycle.

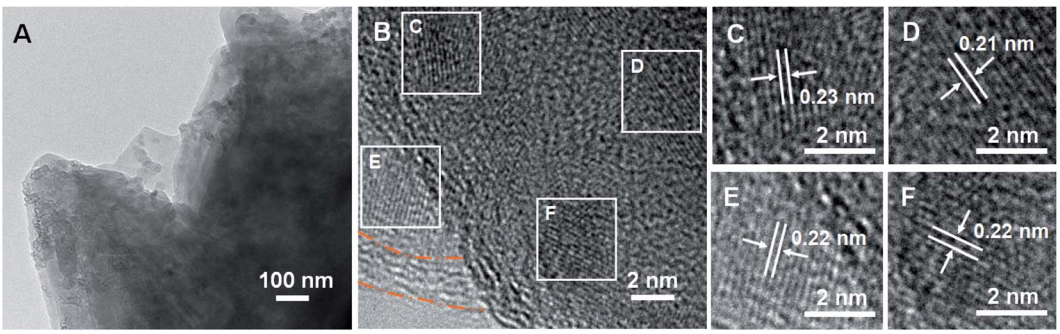

Fig. 6 *Ex situ* TEM (A) and HRTEM (B–F) images of $Fe_2(MoO_4)_3$/C-NS at a cell voltage of 3.0 V after 100 cycles.

of catalyst for the reversible formation of a SEI layer.[13,46] The high ICE value of $Fe_2(MoO_4)_3$/C-NS is connected to the highly reversible transformation of the SEI layer. Furthermore, the reversible evolution of the SEI layer can provide extra electrode capacity, leading to the improved electrochemical performance of $Fe_2(MoO_4)_3$/C-NS.

The structural stability of $Fe_2(MoO_4)_3$/C-NS was investigated through TEM analysis, which was conducted on the electrode at a cell voltage of 3.0 V after 100 cycles. Though some nanoparticles can be observed on the surface of the cycled electrode, the nanosheet structure is mostly maintained (Fig. 6A), illustrating the high stability of the electrode during the electrochemical process. Small nanocrystals can be seen on the surface of the nanosheets in Fig. 6B, and enlarged images are shown in Fig. 6C–F. Nanocrystals with clear spacings of 0.21 and 0.23 nm can be observed in Fig. 6C and D, respectively, which are assigned to the (220) and (−121) planes of monoclinic MoO_3 (JCPDS no. 01-089-1554),[10] while the nanocrystals in Fig. 6E–F with lattice fringes of 0.22 nm could be assigned to the (113) planes of rhombohedral Fe_2O_3 (JCPDS no. 00-001-1053). TEM analysis clearly elucidates the formation of Fe_2O_3 and MoO_3 after the charging process.

4. Conclusions

In summary, we have developed a simple and feasible method to synthesize carbon coated $Fe_2(MoO_4)_3$ nanosheets using urea as the template and carbon source. The *in situ* formed carbon coating on the surface could effectively restrict electrode material volume changes during electrochemical processes and improve the reaction kinetics. Furthermore, the nanosheet structure provides much shorter diffusion distances for charge carriers. Due to this rational design, $Fe_2(MoO_4)_3$/C-NS shows excellent rate capability (a reversible discharge capacity of 983 mA h g^{-1} at 5 A g^{-1}) and outstanding cycling performance (1376 mA h g^{-1} at 0.5 A g^{-1} after 250 cycles, and 864 mA h g^{-1} at 2 A g^{-1} after 500 cycles). Importantly, $Fe_2(MoO_4)_3$/C-NS exhibits a high ICE value (higher than 87%), which can be ascribed to reductions in volume variation during the electrochemical processes due to the carbon coating, as well as a catalysis effect from the generated Fe, leading to reversible SEI layer formation during the charge/discharge process. This simple method could be extended to the synthesis of other carbon coated composites, which could act as promising electrode materials for next-generation energy storage devices.

Conflicts of interest

There are no conflicts of interest to declare.

Acknowledgements

The research was financially supported by the National Natural Science Foundation of China (51572101, 51872107, and 21802050), the Natural Science Foundation of Hubei Province (2018CFB366), and the Fundamental Research Funds for the

Central Universities (2662017QD026, 2662016QD029, 2662015PY047, and 2662016PY088).

References

1 J. B. Zhou, Z. H. Jiang, S. W. Niu, S. S. Zhu, J. Zhou, Y. C. Zhu, J. W. Liang, D. D. Han, K. L. Xu, L. Q. Zhu, X. J. Liu, G. M. Wang and Y. T. Qian, *Chem*, 2018, **4**, 372–385.
2 B. Anasori, M. R. Lukatskaya and Y. Gogotsi, *Nat. Rev. Mater.*, 2017, **2**, 16098.
3 J. Cuan, Y. Zhou, J. Zhang, T. F. Zhou, G. M. Liang, S. Li, X. B. Yu, W. K. Pang and Z. P. Guo, *ACS Nano*, 2019, **13**, 11665–11675.
4 L. T. Yan, X. H. Rui, G. Chen, W. C. Xu, G. F. Zou and H. M. Luo, *Nanoscale*, 2016, **8**, 8443–8465.
5 L. J. Wang, X. H. Cui, L. L. Gong, Z. Y. Lyu, Y. Zhou, W. H. Dong, J. Liu, M. Lai, F. W. Huo, W. Huang, M. Lin and W. Chen, *Nanoscale*, 2017, **9**, 3898–3904.
6 J. J. Deng, X. L. Yu, Y. B. He, B. H. Li, Q. H. Yang and F. Y. Kang, *Energy Storage Materials*, 2017, **6**, 61–69.
7 R. Zhang, X. Huang, D. Wang, T. K. A. Hoang, Y. Yang, X. Duan, P. Chen, L. C. Qin and G. Wen, *Adv. Funct. Mater.*, 2018, **28**, 1705817.
8 K. Chi, Z. Y. Zhang, Q. Y. Lv, C. Y. Xie, J. Xiao, F. Xiao and S. Wang, *ACS Appl. Mater. Interfaces*, 2017, **9**, 6044–6053.
9 A. Pramanik, S. Maiti and S. Mahanty, *Chem. Eng. J.*, 2017, **307**, 239–248.
10 C. Liang, Y. Tao, N. Yang, D. Huang, S. Li, K. Han, Y. Luo, H. Chen and L. Mai, *Electrochim. Acta*, 2019, **311**, 192–200.
11 C. Han, X. Ren, Q. Li, W. Luo, L. Huang, L. Zhou and L. Mai, *Nano Res.*, 2018, **11**, 1285–1293.
12 P. L. Taberna, S. Mitra, P. Poizot, P. Simon and J. M. Tarascon, *Nat. Mater.*, 2006, **5**, 567–573.
13 L. W. Su, Y. R. Zhong and Z. Zhou, *J. Mater. Chem. A*, 2013, **1**, 15158.
14 C. Chen, L. Peng, Y. Li, L. Zhang, J. Xiang, P. Hu, S. Cheng, Y. Huang and J. Xie, *ACS Appl. Mater. Interfaces*, 2017, **9**, 15470–15476.
15 B. Y. Guan, X. Y. Yu, H. B. Wu and X. W. Lou, *Adv. Mater.*, 2017, **29**, 1703614.
16 Z. Ju, E. Zhang, Y. Zhao, Z. Xing, Q. Zhuang, Y. Qiang and Y. Qian, *Small*, 2015, **11**, 4753–4761.
17 H. Zheng, S. Q. Wang, J. Z. Wang, J. Wang, L. Li, Y. Yang, C. Q. Feng and Z. Q. Sun, *J. Nanopart. Res.*, 2015, **17**, 449.
18 S. Yang, W. Dong, D. Shen, S. Li, W. Sun, X. Hong, M. Wang and Y. Mao, *Chem. Eng. J.*, 2017, **309**, 674–681.
19 H. Niu, D. Zhou, X. Yang, X. Li, Q. Wang and F. Y. Qu, *J. Mater. Chem. A*, 2015, **3**, 18413.
20 H. J. Fu, Y. Wang, X. X. Dong, Y. X. Liu, Z. J. Chen, Y. D. Shen, C. Yang, J. X. Dong and Z. L. Xu, *RSC Adv.*, 2016, **6**, 65588.
21 Y. Hong, J. Shi, W. Shi, Z. Fang, R. Chen and Y. Huang, *Carbon*, 2018, **136**, 160–167.
22 Y. X. Yang, L. Geng, Y. N. Guo, J. Q. Meng and Y. H. Guo, *Appl. Surf. Sci.*, 2017, **425**, 535–546.
23 X. Xiang, Z. Wang, X. Shi, M. Fan and X. Sun, *ChemCatChem*, 2018, **10**, 4530–4535.
24 S. Q. Wang, X. Cai, Y. Song, X. Q. Sun and X. X. Liu, *Adv. Funct. Mater.*, 2018, **28**, 1803901.
25 J. S. Park, J. S. Cho and Y. C. Kang, *J. Power Sources*, 2018, **379**, 278–287.
26 Y. T. Zuo, G. Wang, J. Peng, G. Li, Y. Q. Ma, F. Yu, B. Dai, X. H. Guo and C. P. Wong, *J. Mater. Chem. A*, 2016, **4**, 2453–2460.
27 S. Y. Lu, T. X. Zhu, Z. Y. Li, Y. C. Pang, L. Shi, S. J. Ding and G. X. Gao, *J. Mater. Chem. A*, 2018, **6**, 7005–7013.
28 W. Wang, J. W. Qin, Z. G. Yin and M. H. Cao, *ACS Nano*, 2016, **10**, 10106–10116.
29 W. Han, X. Qin, J. Wu, Q. Li, M. Liu, Y. Xia, H. Du, B. Li and F. Kang, *Nano Res.*, 2017, **11**, 892–904.
30 V. K. Mariappan, K. Krishnamoorthy, P. Pazhamalai, S. Sahoo, D. Kesavan and S. J. Kim, *J. Power Sources*, 2019, **433**, 126648.
31 Y. W. Cheng, S. T. Lu, H. B. Zhang, C. V. Varanasi and J. Liu, *Nano Lett.*, 2012, **12**, 4206–4211.
32 H. Hu, J. Zhang, B. Guan and X. W. Lou, *Angew. Chem., Int. Ed.*, 2016, **55**, 9514–9518.
33 Z. Yao, X. Xia, C. A. Zhou, Y. Zhong, Y. Wang, S. Deng, W. Wang, X. Wang and J. Tu, *Adv. Sci.*, 2018, **5**, 1700786.
34 L. Zhang, S. S. Zheng, L. Wang, H. Tang, H. G. Xue, G. X. Wang and H. Pang, *Small*, 2017, **13**, 1700917.
35 Y. Zhu, A. Hu, Q. Tang, S. Zhang, W. Deng, Y. Li, Z. Liu, B. Fan, K. Xiao, J. Liu and X. Chen, *ACS Appl. Mater. Interfaces*, 2018, **10**, 8955–8964.
36 H. Zhang, R. Hu, Y. Liu, X. Cheng, J. Liu, Z. Lu, M. Zeng, L. Yang, J. Liu and M. Zhu, *Energy Storage Materials*, 2018, **13**, 257–266.
37 T. Liang, R. Hu, H. Zhang, H. Zhang, H. Wang, Y. Ouyang, J. Liu, L. Yang and M. Zhu, *J. Mater. Chem. A*, 2018, **6**, 7206–7220.
38 Y. Jin, S. Li, A. Kushima, X. Q. Zheng, Y. M. Sun, J. Xie, J. Sun, W. J. Xue, G. M. Zhou, J. Wu, F. F. Shi, R. F. Zhang, Z. Zhu, K. So, Y. Cui and J. Li, *Energy Environ. Sci.*, 2017, **10**, 580–592.
39 S. H. Yan, K. P. Abhilash, L. Y. Tang, M. Yang, Y. F. Ma, Q. Y. Xia, Q. B. Guo and H. Xia, *Small*, 2019, **15**, 1804371.
40 J. Nzabahimana, S. T. Guo and X. L. Hu, *Appl. Surf. Sci.*, 2019, **479**, 287–295.
41 W. H. Li, S. H. Hu, X. Y. Luo, Z. L. Li, X. Z. Sun, M. S. Li, F. F. Liu and Y. Yu, *Adv. Mater.*, 2017, **29**, 1605820.
42 J. Z. Li, H. Li, Z. X. Wang, L. Q. Chen and X. J. Huang, *J. Power Sources*, 2002, **107**, 1–4.
43 H. Ota, Y. Sakata, A. Inoue and S. Yamaguchi, *J. Electrochem. Soc.*, 2004, **151**, A1659–A1669.
44 M. Y. Nie and B. L. Lucht, *J. Electrochem. Soc.*, 2014, **161**, A1001–A1006.
45 A. S. Cavanagha, Y. Lee, B. Yoon and S. George, *J. Electrochem. Soc.*, 2010, **33**, 223–229.
46 L. W. Su, Z. Zhou and P. W. Shen, *Electrochim. Acta*, 2013, **87**, 180–185.